



HAL
open science

Magnetic Anomalies in Five Lunar Impact Basins: Implications for Impactor Trajectories and Inverse Modeling

L. Hood, J. Oliveira, J. Andrews-hanna, M. Wieczorek, S. Stewart

► **To cite this version:**

L. Hood, J. Oliveira, J. Andrews-hanna, M. Wieczorek, S. Stewart. Magnetic Anomalies in Five Lunar Impact Basins: Implications for Impactor Trajectories and Inverse Modeling. *Journal of Geophysical Research. Planets*, 2021, 126 (2), 10.1029/2020JE006668 . hal-03365601

HAL Id: hal-03365601

<https://hal.science/hal-03365601>

Submitted on 12 Aug 2022

HAL is a multi-disciplinary open access archive for the deposit and dissemination of scientific research documents, whether they are published or not. The documents may come from teaching and research institutions in France or abroad, or from public or private research centers.

L'archive ouverte pluridisciplinaire **HAL**, est destinée au dépôt et à la diffusion de documents scientifiques de niveau recherche, publiés ou non, émanant des établissements d'enseignement et de recherche français ou étrangers, des laboratoires publics ou privés.

Copyright

Key Points:

- Based on a recent field map, five lunar impact basins containing magnetic anomalies dating from the time of basin formation are identified
- Assuming that these anomalies are due to impactor-added iron, inferences are drawn about the trajectories of the basin-forming impactors
- Inverse modeling of the anomalies yields results that are difficult to reconcile with the centered, axially aligned core dynamo hypothesis

Supporting Information:

Supporting Information may be found in the online version of this article.

Correspondence to:

L. L. Hood,
lon@lpl.arizona.edu

Citation:

Hood, L. L., Oliveira, J. S., Andrews-Hanna, J., Wieczorek, M. A., & Stewart, S. T. (2021). Magnetic anomalies in five lunar impact basins: Implications for impactor trajectories and inverse modeling. *Journal of Geophysical Research: Planets*, 126, e2020JE006668. <https://doi.org/10.1029/2020JE006668>

Received 25 AUG 2020

Accepted 13 DEC 2020

Magnetic Anomalies in Five Lunar Impact Basins: Implications for Impactor Trajectories and Inverse Modeling

L. L. Hood¹ , J. S. Oliveira^{2,3} , J. Andrews-Hanna¹ , M. A. Wieczorek⁴ , and S. T. Stewart⁵ 

¹Lunar and Planetary Laboratory, University of Arizona, Tucson, AZ, USA, ²ESA/ESTEC, SCI-S, Noordwijk, Netherlands, ³Department of Payloads and Space Sciences, Space Magnetism Area, National Institute for Aerospace Technology, Torrejón de Ardoz, Spain, ⁴Observatoire de la Côte d'Azur, CNRS, Laboratoire Lagrange, Université Côte d'Azur, Nice, France, ⁵Department of Earth and Planetary Sciences, University of California, Davis, CA, USA

Abstract A recent large-scale map of the lunar crustal magnetic field is examined for the existence of magnetic anomalies internal to ringed impact basins. It is found that, of 25 basins with upper preNectarian and younger ages, 18 contain mapped internal anomalies with amplitudes of at least 1 nT at 30 km altitude. Of these, five are most confidently judged to contain intrinsic anomalies (i.e., anomalies located within the inner basin rims and originating at the times of basin formation): Crisium, Humboldtianum, Mendel-Rydberg, Moscoviense, and Nectaris. Comparing the anomaly distributions with previous numerical simulations of the impact of iron-rich planetesimals to form a large (SPA-sized) basin, inferences are drawn about the likely trajectories of the impactors. Specifically, results suggest that impactor trajectories for these basins were within $\sim 45^\circ$ of being vertical and tended to lie on average parallel to the lunar equatorial plane and the ecliptic plane. Inverse modeling of anomalies within these basins yields inferred directions of magnetization that are difficult to reconcile with the axial centered dipole hypothesis for the geometry of the internal lunar dynamo field: Paleomagnetic pole positions are widely scattered and, in agreement with a recent independent study, the two main anomalies within Crisium yield significantly different directions of magnetization.

Plain Language Summary Magnetic anomalies in lunar impact basins are especially important because the interiors of the basins cooled very slowly requiring a steady, long-lived magnetizing field to impart magnetization. They are the best orbital evidence for a former internal lunar dynamo field. In this study, five basins are selected that most confidently contain internal anomalies that are intrinsic to the basin, i.e., located within the inner basin rims and originating at the times of basin formation. Assuming that these internal anomalies are due to magnetization of impact melt containing iron from the impactor that created the basins, comparisons are made with previous numerical simulations to constrain the trajectories of the impactors. Results suggest that the five impactor trajectories were within roughly 45 degrees of being vertical and tended to lie on average parallel to the lunar equatorial plane and the ecliptic plane. Inverse modeling of the anomalies yields inferred directions of magnetization that are difficult to reconcile with the hypothesis that the lunar dynamo field originated in the small metallic core. Possible explanations include that the core dynamo behaved unlike the current terrestrial dynamo or that the magnetizing field was instead due to dynamo generation in an early shallow magma ocean.

1. Introduction

Magnetic anomalies within large lunar impact basins that date from the time of formation of the basins (referred to here as “intrinsic internal magnetic anomalies”) are of special interest because their sources are most likely to have formed via cooling through the Curie blocking temperature in the presence of an ambient magnetic field (i.e., thermoremanent magnetization, or TRM). This is in contrast to anomalies in the highlands, which could have sources consisting of impact ejecta materials whose magnetization could have been acquired by shock in a short-lived ambient field whose direction differed from that of the internal lunar field (Gattacceca et al., 2010; Hood & Artemieva, 2008; but see also Oran et al. [2020]).

The first comprehensive survey of magnetic fields of lunar multiring impact basins was made using Lunar Prospector (LP) electron reflection data (Halekas et al., 2003). It was found that the primary magnetic

signature of lunar basins is a magnetic low, suggesting shock demagnetization. However, like terrestrial impact basins (e.g., Hart et al., 1995; Pilkington & Grieve, 1992), a secondary magnetic signature was found in many basins consisting of anomalies within the main rim. The existence of internal basin anomalies was shown to be a function of relative age with the oldest (preNectarian) basins having no signatures, the less old (Nectarian) basins having the strongest signatures, and the youngest (Imbrian) basins having very weak signatures. A later survey of LP magnetometer data found supporting evidence that anomalies are present within the inner rims of the Nectarian-aged Moscoviense, Mendel-Rydberg, Humboldtianum, and Crisium basins (Hood, 2011).

Numerical impact simulations show that, for impact angles within $\sim 45^\circ$ of the vertical, lunar impact basins will contain thick deposits of impact melt that are enriched in iron from the impactor (Wieczorek et al., 2012). Also, some terrestrial impact structures such as Chicxulub contain a substantial amount of impact melt within an annular ring outside of the peak ring. Such deposits should have acquired coherent magnetization if a steady, long-lived magnetizing field existed as they slowly cooled. Laboratory analyses of returned samples provide evidence that such an internal field was present during the basin-forming epoch (for a review, see Weiss and Tikoo [2014]). An alternate model involving shock-induced melting and rapid TRM acquisition in the upper crust caused by a transient field produced in the impact has recently been studied quantitatively (Crawford, 2015, 2020). However, this model predicts that the largest lunar basins will contain the strongest magnetizations. It therefore does not easily explain the observation that the youngest large basins (Imbrium and Orientale) have almost no detectable anomalies in their interiors (e.g., Hood & Spudis, 2016).

The strongest lunar magnetic anomalies are found outside of impact basins. The origin of these strong anomalies remains controversial with some authors suggesting igneous sources (e.g., Hemingway & Tikoo, 2018; Purucker et al., 2012) and others suggesting sources in the form of coherently magnetized deposits of impact basin ejecta (Hood et al., 2001, 2013; Richmond et al., 2003; Wieczorek et al., 2012). Recent work reported in a companion paper provides new evidence in favor of the impact basin ejecta hypothesis (Hood et al., 2021).

Although the numerical simulations of Wieczorek et al. (2012) were done for the special case of the impact that produced the South Pole-Aitken (SPA) basin, many aspects of their results for different impactor sizes, iron contents, and impact angles, are likely to be applicable to smaller lunar basin-forming impacts (see their Figure 3 and the supporting online material). According to these simulations, the absence of anomalies within some impact basins could be due either to a weak ambient magnetic field when these basins formed, or to an iron-poor impactor (as an extreme example, a cometary nucleus), or to an oblique impact angle, which would have deposited the iron as ejecta well outside of the basin. Oliveira et al. (2017) have developed a technique based on laboratory measurements to infer the average abundances of projectile metallic iron in lunar impact basin melt sheets of given thicknesses. The impactor-added iron model for the origin of internal basin anomalies has recently been applied to interpret observations of magnetic anomalies within impact basins on Mercury (Hood et al., 2018).

If intrinsic internal basin anomalies have sources in the form of impact melt that was enriched in impactor iron and subsequently magnetized in a steady internal magnetic field, at least two applications of these anomalies are possible. First, the distribution of magnetic anomalies within a given basin may, when combined with the simulation results of Wieczorek et al. (2012), provide useful constraints on the trajectory of the impactor. Second, if the anomaly sources were magnetized by TRM in an internal, steady magnetic field, the directions of magnetization of these sources would provide information on the configuration of the internal magnetizing field (e.g., Weiss & Tikoo, 2014).

Because the lunar metallic core is relatively small, higher-order moments of the core field would decay more rapidly with distance so a core dynamo magnetizing field would be expected to be dominantly dipolar in orientation at the surface. Core dynamo models generally predict an approximate alignment of the dynamo magnetic dipole moment with the rotation axis, as is true for the Earth's field. Barring a large amount of true polar wander, inversions of these basin anomalies would therefore provide at least a moderate test of the core dynamo hypothesis. Specifically, inferred directions of magnetization can be used to calculate paleomagnetic pole positions, which should show some clustering if the above assumptions are valid. Even if

the dynamo reversed its orientation from time to time, as does the Earth's dynamo, some clustering should be found in opposite hemispheres.

Lunar magnetic anomalies (including those within impact basins) have previously been modeled by many authors for the purpose of constraining the former core dynamo and/or the occurrence of true lunar polar wander (Baek et al., 2019; Oliveira & Wieczorek, 2017; and references therein). However, this work has been far from conclusive with proposed clustering of paleomagnetic poles in at least three different locations (Arkani-Hamed & Boutin, 2014; Takahashi et al., 2014; Tsunakawa et al., 2010). Oliveira and Wieczorek (2017) used the gridded magnetic field models of Tsunakawa et al. (2010) and found paleomagnetic pole positions at both polar and equatorial latitudes with some preference at 90° east and west longitudes. The current work is intended to complement these prior efforts by implementing the following three improvements: First, a recent large-scale map of the lunar crustal magnetic field is applied to allow a re-evaluation of those basins that are most confidently considered to contain true intrinsic internal anomalies. Only these latter anomalies, whose sources are most likely to have acquired magnetization by slow cooling in the former lunar internal magnetic field, are subjected to modeling analyses. Second, only the best direct measurements are employed for the modeling analyses (i.e., not a field model; lowest altitude direct magnetometer data with least amount of external field contamination over a given basin). Third, Parker's inversion method (Parker, 1991), which has a number of advantages over alternate methods (see Section 4 below), is employed.

In Section 2, a newly constructed large-scale map of the lunar crustal field is used together with regional maps and direct radial field measurements along individual orbit passes to identify those basins whose internal anomalies can most confidently be classified as intrinsic. In Section 3, refined regional maps of the basins with probable intrinsic anomalies are constructed and are applied together with the numerical simulation results of Wieczorek et al. (2012) to constrain impactor trajectories for those basins. In Section 4, inversion modeling is conducted of the anomalies within the selected basins. A summary and discussion are given in Section 5.

2. Re-evaluation of Intrinsic Internal Anomalies

In order to evaluate whether anomalies observed to be internal to the rim of a basin are intrinsic to the basin (or are instead due for instance to superposed magnetized ejecta from a later basin-forming event), it is necessary to consider the overall distribution of anomalies around the basin. For this purpose, we make use of a recently constructed large-scale map of the crustal field covering most latitudes of interest (Hood et al., 2021). As described in the latter reference, the mapping approach used an overlapping regional technique that selected only the best measurements over a given region before combining the regional maps to produce a large-scale map.

The final contour map of the field magnitude at 30 km altitude above the mean lunar radius (from Figure 5 of Hood et al. [2021]) is reproduced in Figure S1 of the supporting material. It was produced using an iterative equivalent source dipole (ESD) technique described originally by Hood (2015) with minor updates given in (Hood et al., 2016, 2015). The contour interval is 1 nT, which is the approximate effective noise level. It is superposed on a Lunar Reconnaissance Orbiter Wide Angle Camera (WAC) shaded relief map using topography derived from Lunar Reconnaissance Orbiter Laser Altimeter (LOLA) data (Smith et al., 2010). The map has general characteristics consistent with previous large-scale maps of the lunar crustal field. In particular, fields are relatively weak across the north-central near side and across the north-central far side. The nearside magnetic low region coincides approximately with the Procellarum-KREEP Terrane (PKT), suggesting that its higher abundance of heat-producing elements may have thermally demagnetized the region over time (Wieczorek, 2018). In the remainder of this section, this map is applied to classify lunar impact basins as (a) containing internal anomalies and (b) containing internal anomalies that are intrinsic to the basin. In the following, "altitude" means altitude above the mean lunar radius of 1,737.4 km.

Internal anomalies are defined as anomalies within a basin's main rim that are confirmed to be of lunar origin by repetition on successive orbits. As stated in the Introduction, intrinsic internal anomalies are defined as those internal anomalies within a basin that date from the time of formation of the basin. While absolute identification of such anomalies is not possible using orbital data alone, several criteria can be used to

increase the probability of successful identifications. These criteria are: (1) The anomalies should lie within the inner rim where numerical simulations show impact melt containing impactor iron to be concentrated for nonoblique impacts; (2) they should have a mapped amplitude of at least 2 times the noise level (~ 2 nT at 30 km altitude) to allow meaningful inversion modeling; (3) they should not connect to other anomalies outside of the inner rim with an amplitude larger than the map noise level (~ 1 nT); and (4) they should not have any apparent relationship (e.g., radial alignments) with nearby younger basins.

Columns 1–4 of Table 1 list in order of increasing relative age 25 candidate lunar basins, their center locations, main ring diameters and relative ages within the Imbrian (I), Nectarian (N), and preNectarian (pN) groups according to the original tabulation of Wilhelms (1984; see his Table 6.4). More recent work (e.g., Neumann et al., 2015) has refined the identification and sizes of main, intermediate, and inner rings of these basins using LOLA topography. Also, Fassett et al. (2012) have applied more complete superposed crater size-frequency distributions derived from LOLA data to refine these age estimates. In most cases, results agree with those of Wilhelms (1984) but some differences are notable. For example, they suggest that Serenitatis is older than Nectaris and Humboldtianum is younger than Crisium. Included in Table 1 are the 25 basins with estimated relative ages as young or younger than that of the preNectarian Coulomb-Sarton basin (see Halekas et al. [2003] for a similar listing). Impact basins (as opposed to impact craters) are normally defined as having main rim diameters of 300 km or more. However, one large crater (Leibnitz, diameter 245 km) is added to the table since it is relatively large and contains an internal anomaly.

The fifth column of the table contains an assessment of whether true internal magnetic anomalies (i.e., those that are genetically associated with the basin) are present within the main rims of the basins. In each case, in addition to studying mapped anomalies (the large-scale map of Figure S1 and other regional maps), all available radial field component magnetometer data from either the LP or Kaguya (KG) polar orbital missions were re-examined to determine if anomalies of lunar origin (i.e., those that approximately repeat on successive orbits) are present within a given basin. In column 5, we first indicate whether such anomalies were detectable at the lowest measurement altitudes. If internal anomalies were detected, then we further indicate in parentheses whether they are clearly intrinsic to the basin according to the above criteria.

2.1. Imbrian Basins

For the youngest (Imbrian-aged) basins, a previous study has shown that internal anomalies were not detectable within Orientale but that weak internal anomalies are present within the main rims of Schrödinger and Imbrium (Hood & Spudis, 2016). One of these basins (Imbrium) lies within the PKT, which is generally weak magnetically. The second-youngest basin, Schrödinger, contains anomalies with amplitudes approaching 2 nT at 20 km altitude distributed asymmetrically on the northwest side of the basin interior. Imbrium contains only a single isolated anomaly located in the south-central part of the basin interior with smoothed amplitude ~ 2 nT at an altitude of less than 15 km. The latter anomaly is not seen in Figure S1 because it has a mapped amplitude of less than 1 nT at 30 km altitude. As indicated in column 5 of the table, of these three basins, only Imbrium and Schrödinger are assessed as containing detectable internal anomalies. The internal anomalies within Schrödinger are not clearly intrinsic because they appear to be connected to anomalies outside the basin rim (see Figure 5 of Hood and Spudis [2016]). The single anomaly in Imbrium is not connected to anomalies outside of the basin rim but has a mapped amplitude in Figure S1 of less than 1 nT. The intrinsic assessment for Imbrium is therefore uncertain as indicated in the table.

2.2. Nectarian Basins

Of the Nectarian-aged basins listed in Table 1, all but one (Bailly) lie completely within the boundaries of Figure S1. None of the Nectarian-aged basins lies within the generally low field zones (the PKT and the north-central far side zone) identified by Wieczorek (2018). An examination of KG radial component stack plots over Bailly and regional mapping of the field magnitude over this basin shows that a broad internal anomaly is present centered not far from the basin center. However, this anomaly could be connected to a large mass of stronger anomalies just south of the basin rim. The existence of intrinsic anomalies within Bailly is therefore conservatively assessed as uncertain in the table.

Table 1
Internal Magnetic Anomalies in Post Coulomb-Sarton Lunar Impact Basins^a

Basin name	Center location	Main ring diameter, km	Relative age	Internal anomalies? (intrinsic?)
Orientele	265°E, 20°S	930	I-1	No
Schrödinger	134°E, 75°S	320	I-2	Yes (?)
Imbrium	342°E, 33°N	1,200	I-3	Yes (?)
Bailly	292°E, 67°S	300	N-4	Yes (?)
Hertzprung	231°E, 2°N	570	N-4	No
Serenitatis	19°E, 27°N	740	N-4	Yes (?)
Crisium	59°E, 18°N	635	N-4	Yes (Yes)
Humorum	320°E, 24°S	440	N-4	Yes (?)
Humboldtianum	84°E, 61°N	600	N-5	Yes (Yes)
Mendelev	141°E, 6°N	330	N-6	No
Mendel-Rydberg	266°E, 50°S	630	N-6	Yes (Yes)
Korolev	203°E, 5°S	440	N-6	No
Moscoviense	147°E, 26°N	445	N-6	Yes (Yes)
Nectaris	34°E, 16°S	860	N-6	Yes (Yes)
Leibnitz	179°E, 38°S	245	N-6	Yes (?)
Apollo	209°E, 36°S	505	pN-7	Yes (?)
Grimaldi	291°E, 6°S	430	pN-7	No
Freundlich-Sharanov	175°E, 19°N	600	pN-8	Yes (?)
Birkhoff	213°E, 59°N	330	pN-9	No
Planck	136°E, 58°S	325	pN-9	Yes (?)
Schiller-Zucchi	315°E, 56°S	325	pN-9	Yes (?)
Amundsen-Ganswindt	120°E, 81°S	355	pN-9	Yes (?)
Lorentz	263°E, 34°N	360	pN-10	Yes (?)
Smythii	87°E, 2°S	840	pN-11	Yes (?)
Coulomb-Sarton	237°E, 52°N	530	pN-11	No

Note. Relative ages in column 4 are based on Wilhelms [1984].

Abbreviation: I, Imbrian; N, Nectarian; pN, preNectarian.

^aThese evaluations are done using maps constructed at 30 km altitude. Internal anomalies are defined as any anomalies of lunar origin located within the inner basin rim. Intrinsic anomalies are those that are clearly associated with the basin itself (see the criteria given in the text).

Three Nectarian-aged basins have no detectable anomalies that are clearly inside their main rims: Hertzprung, Mendelev, and Korolev. Several other Nectarian-aged basins have internal anomalies that are not judged to be clearly intrinsic: Serenitatis, Humorum, and Leibnitz. As seen in Figure S1, Humorum possesses an anomaly centered just inside the northwest rim. However, this anomaly appears to extend across the rim and is not unlike many other anomalies in the southern Procellarum region. Leibnitz possesses internal anomalies including one located very close to the basin center. However, these anomalies are connected to other stronger anomalies outside of the basin that are part of the northwest SPA (Imbrium antipode) group. Serenitatis has several internal anomalies as seen in Figure S1 but the southernmost ones extend across the main basin rim. Also, the southern anomalies in Serenitatis extend radially away from Imbrium suggesting deposition of ejecta from that younger basin. The northern Serenitatis anomaly is a better candidate for an intrinsic anomaly but is connected to the southern anomalies. These internal anomalies are therefore uncertain to be intrinsic, as indicated in column 5 of the table.

The remaining five Nectarian-aged basins have internal anomalies with characteristics that are most consistent with being intrinsic: Crisium, Humboldtianum, Mendel-Rydberg, Moscoviense, and Nectaris. Three

of these (Humboldtianum, Mendel-Rydberg, and Moscoviense) have centrally located anomalies that are clearly stronger than and not significantly connected to other anomalies outside their rims. Crisium has two symmetrically located main anomalies inside its inner rim on the northern and southern sides of the basin that are much stronger than any anomalies adjacent to the basin. Nectaris has internal anomalies inside its inner rim with peak amplitude only slightly more than 2 nT at 30 km altitude (slightly weaker than those in Humboldtianum). These anomalies are distributed across most of the basin interior but are not connected to anomalies outside of the basin. They are therefore judged to be intrinsic to the basin.

Among the Nectarian-aged basins, there is no obvious dependence of internal anomaly amplitudes on basin size, structure, or relative age. For example, Hertzprung is about half as large as Crisium and both basins are late Nectarian in age but Hertzprung has no detectable internal anomalies while Crisium has relatively strong internal anomalies. Also, Moscoviense is only about half as large as Nectaris and both basins are early Nectarian in age but anomalies in Moscoviense are about 2 times stronger than those in Nectaris. Three of the five basins (Crisium, Nectaris, and Mendel-Rydberg) are considered to be certain or probable multiringed basins according to an assessment by Neumann et al. (2015). Humboldtianum may also be a multiringed basin although the evidence for a third ring is weak. On the other hand, the Nectarian-aged Hertzprung basin is considered to be a probable multiringed basin but has no detectable anomalies in its interior. Moscoviense with a main ring diameter of 445 km is the smallest of the basins with intrinsic anomalies and is classified as a peak-ring basin by Neumann et al. (2015).

2.3. PreNectarian Basins

In the case of the ten preNectarian basins listed in Table 1, three (Grimaldi, Birkhoff, and Coulomb-Sarton) have no detectable internal anomalies while the remaining seven have internal anomalies that are not clearly intrinsic. As seen in Figure S1, most of the latter basins have internal anomalies that are not clearly separated from anomalies lying just outside of the basin rims. For example, the Apollo basin lies within the northeast rim of SPA adjacent to large masses of strong anomalies centered on the Serenitatis and Crisium antipodes. Freundlich-Sharanov has weak anomalies inside its southwestern rim but these are not clearly distinct from similar anomalies in the adjacent highlands. Similarly, Planck, Schiller-Zuchius, Lorentz, and Smythii have anomalies in their interiors that are not clearly separated or distinct from nearby anomalies outside the basin rims. Finally, Amundsen-Ganswindt lies adjacent to Schrödinger and its internal anomalies are part of a mass of strong anomalies that extend to the rim of Schrödinger (see Figure 5 of Hood and Spudis [2016]).

It is noteworthy that two of the three preNectarian basins with no detectable internal anomalies (Birkhoff and Coulomb-Sarton) lie in the north-central far side zone of generally low fields recognized by Wicczorek (2018). However, this is not a zone with a high abundance of heat-producing elements so its origin is unclear. It may have simply escaped substantial deposition of iron-enriched ejecta from younger basin-forming impacts.

3. Implications for Impactor Trajectories

Wicczorek et al. (2012) have reported modeling of the formation of a large lunar basin (SPA) via the impact of iron-rich planetesimals using a CTH shock physics code in three dimensions with self-gravity. A variety of impact parameters and velocities ranging from 10 to 30 km/sec were considered. It was found that, for near-vertical impacts (impact angles less than 30° from the vertical), most of the projectile core materials were deposited close to the center of the basin. For moderately oblique impacts (e.g., 30°–45° from vertical), most of the impactor iron was deposited within the inner basin rim on the downrange side. For very oblique impacts (e.g., 60° from vertical), nearly all of the iron was mixed into ejecta that was deposited outside of the inner rim in the downrange direction. The most probable impact angle for a randomly incident body is 45° (Gilbert, 1893; Shoemaker, 1962). Taking the numerical results of Wicczorek et al. (2012) to apply to all lunar basins, approximately half of all basin-forming impacts would therefore be expected to produce iron-enriched impact melt within their inner rims.

As stated in the Introduction, many aspects of the results of Wicczorek et al. (2012) should be applicable to a wide range of lunar basin-forming impacts. However, several caveats regarding this application

should be emphasized. First, these simulations were for an unusually large lunar impact basin (SPA). While simulations for smaller basins should give qualitatively similar results, the details may be different. In particular, planetary curvature would have a greater effect for an SPA-sized basin than for a basin as small as Moscoviense. Therefore, their extrapolation to smaller lunar basins and the specific interpretation of magnetic anomaly distributions in terms of impact angles should be done with caution. Second, the Wieczorek et al. simulations for differentiated impactors considered only a narrow range of iron mass fractions (~ 0.5). A wider range in iron content of basin-forming impactors is likely due to collisional evolution of differentiated planetesimals (e.g., Carter et al., 2015). New simulations would be required to determine the effect of smaller or larger iron mass fractions on the distribution of iron-enriched ejecta and melt.

In the previous section, five basins were found to have internal anomalies with characteristics most consistent with an intrinsic origin. In this section, we assume that the magnetic anomaly sources within these basins consist of iron-enriched impact melt beneath the visible mare basalt surface within the basin interiors. We then compare the implied iron distribution to the numerical simulations summarized above to constrain the trajectories of the impactors that created the basins. We note that all of the considered basins have prominent central Bouguer gravity anomalies. The gravity anomalies are likely a consequence of mantle uplift following the impact and therefore do not provide direct information on the distribution of impactor iron. However, they are very relevant to this study because they are the best indicator of the central depression of the basin, within which impact melt should pool and within which projectile core materials might be expected to be found (based on Figure 3 of Wieczorek et al. [2012]).

3.1. Crisium

Crisium is one of three “certain” multiringed (3 or more rings) basins on the Moon (Neumann et al., 2015; see their Figure S10). In contrast to the 635 km main rim diameter listed by Wilhelms (1984), Neumann et al. list a main ring diameter of 1,076 km and an inner ring diameter of 505 km for this basin. The inner ring, which roughly bounds the Mare Crisium basalt surface, is most relevant to this study since the pool of impact melt would lie within this ring, while the ejecta deposits would begin outside the inner ring but inside the main rim.

Figure 1a is a map of the field magnitude in equirectangular projection over shaded relief within a 40° latitude by 40° longitude region centered on Crisium. The contour interval is 1 nT. A color scale for the topography is provided in Figure S17. The map was produced using methods similar to those applied to produce the large-scale map of Figure S1. However, in order to resolve more details of the anomaly distribution, data selection differed slightly and the ESD method was geared specifically to this region. LP data from March of 1999 were employed and the ESD array consisted of 61 by 61 dipoles $\frac{2}{3}^\circ$ apart in latitude and longitude. Trial calculations for different array depths yielded a minimum root-mean-square (RMS) deviation for a depth of 10 km. The mapping altitude was reduced to 25 km to further resolve the anomaly distribution. The peak amplitude of the northern anomaly at this altitude is about 9 nT.

As seen in Figure 1a, the two strongest anomalies are located on the northern and southern sides of the inner ring interior but are connected by a band of weaker anomalies on the western side of the inner ring. For comparison, the simulations of Wieczorek et al. (2012) for a moderate impact angle produced a concentration of metallic iron on the downrange side of the inner ring. The iron distribution implied by the Crisium anomalies is therefore somewhat unlike that predicted by the Wieczorek et al. (2012) models. Nevertheless, there is at least some bias of the distribution toward the western side of the basin. If the sources are iron-enriched impact melt, the trajectory of the impactor that would be most consistent with the impact simulations is approximately east-northeast to west-southwest at an angle of less than roughly 45° from the vertical. This differs from previous suggestions of a west to east trajectory (e.g., Schultz & Stickle, 2011), which were based partly on the interpretation of the elongated extension on the east side of the basin as being a result of a west to east oblique impact. However, an alternate interpretation of the eastward extension is that it represents a second smaller basin (“Crisium East”) (Frey, 2011; Neumann et al., 2015). The latter authors show evidence for a secondary Bouguer gravity anomaly to support the proposed existence of Crisium East. The trajectory inferred here would also support that interpretation. In any case, a trajectory that was not far from the lunar equatorial plane and ecliptic (whether west-to-east to produce an eastern elongation or east-northeast to west-southwest as suggested here) is indicated.

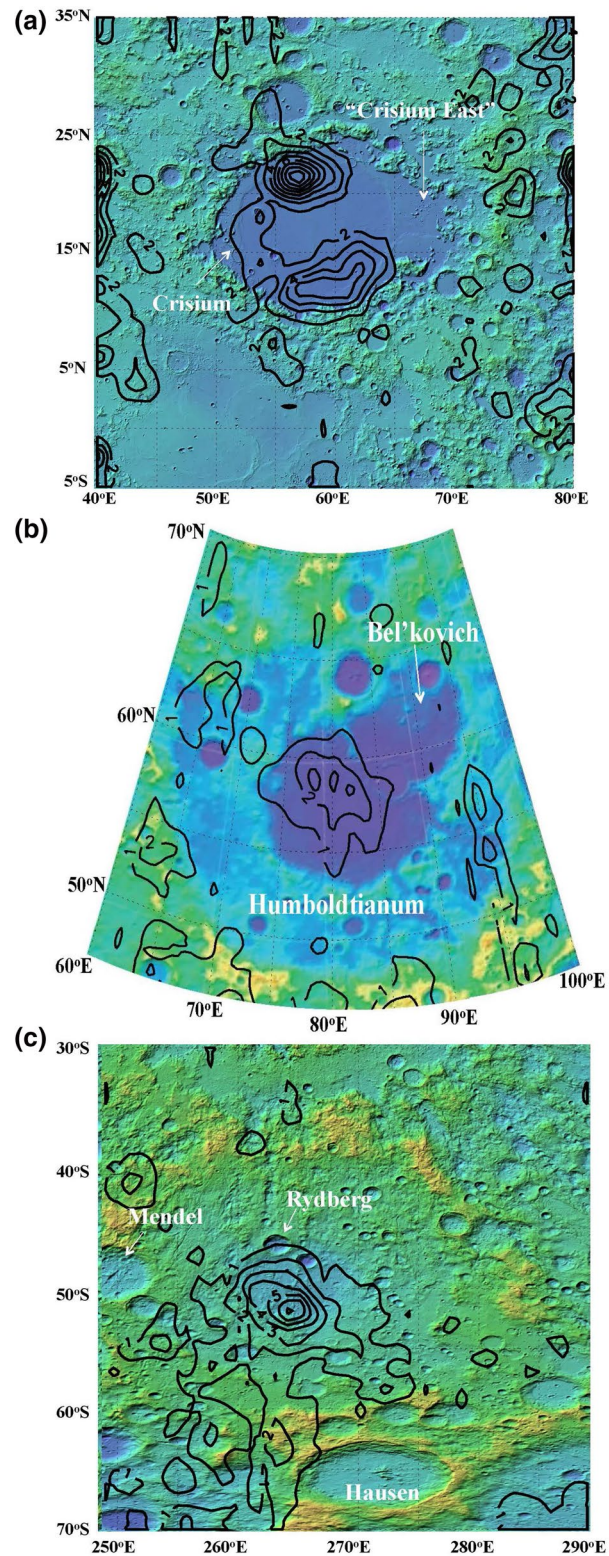


Figure 1. Field magnitude at 25 km over 3 Nectarian-aged lunar impact basins with relatively certain intrinsic internal anomalies: (a) Crisium; (b) Humboldtianum; and (c) Mendel-Rydberg. The contour interval is 1 nT. Superposed on Lunar Reconnaissance Orbiter Laser Altimeter (LOLA) topography over LROC WAC shaded relief. For a color scale, see Figure S17.

3.2. Humboldtianum

The main ring diameter of 600 km for this basin in Table 1 agrees with the estimate of 618 km given by Neumann et al. (2015), who also give an inner ring diameter of 310 km. The inner ring bounds both the mare surface and the positive Bouguer gravity anomaly, which identifies the inner depression where impact melt would be located.

Figure 1b is a map of the field magnitude in orthographic projection over shaded relief covering a region including Humboldtianum. The ESD dipole array consisted of a set of 51 by 41 dipoles spaced 0.5° apart in latitude and 1.0° apart in longitude covering latitudes from 45°N to 70°N and 60°E to 100°E . LP data from April 1999 (April 6, 19.7 h to April 10, 12.9 h) were employed. The spacecraft altitude was in the range of 31–33 km. The dipole array depth was 10 km and the mapping altitude was 25 km.

As seen in the figure, the anomaly amplitude is slightly larger (~ 3 nT) and the anomaly distribution differs slightly from that shown in Figure S1, which was produced from LP data obtained in March 1999 using a different model dipole array spacing. Nevertheless, the anomalies within the inner basin rim remain separated from adjacent anomalies outside the main rim. Anomalies are centered west of the center of the inner ring over the enclosed mare basalt surface. A smaller superposed basin (Bel'kovich) is centered at about 90°E , 62°N .

Although the anomalies peak northwest of the center of the inner rim, it is uncertain whether this is a consequence of the impactor trajectory alone or of later shock demagnetization of the eastern side of the basin by the impact that created the smaller superposed basin. The distribution is therefore judged to be consistent with a nearly vertical impact but impact angles up to $\sim 45^\circ$ from vertical and a southeast to northwest trajectory are allowed.

3.3. Mendel-Rydberg

Mendel-Rydberg is considered to be a “probable” multi-ringed basin by Neumann et al. (2015) with a main ring diameter of 650 km, which agrees with the 630 km listed in Table 1. An intermediate ring diameter of 485 km and a probable 325 km diameter inner peak ring are also identified by the latter authors (see their Figure S8). A Bouguer gravity anomaly occupies most of the region bounded by the inner peak ring.

Figure 1c is a map similar to that of Figure 1a but showing the field magnitude in a 40° by 40° region centered on the Mendel-Rydberg impact basin. Like the map of Figure S1 in this region, the map of Figure 1c was produced using KG data from May of 2009 (May 25, 21.8 h to May 28, 23.2 h). The ESD dipole array again consisted of 61 by 61 dipoles spaced 0.67° apart in latitude and longitude. The preferred depth of the array was again 10 km and the mapping altitude was 25 km. The chosen dipole spacing is not ideal for a high-latitude map because the longitudinal distance between dipoles varies from about 8.3 km at 65°S to 14.5 km at 40°S while the latitudinal spacing is constant at about 20 km. However, repetition of the mapping using a more equidistant dipole spacing of 0.5° in latitude by 1° in longitude produces nearly identical results.

As seen in the figure, the anomaly consists of one broad maximum with a peak amplitude of 7 nT at 25 km altitude. It lies well within the inner peak ring and is displaced slightly southwest of the center. The implicated impactor trajectory is therefore nearly vertical ($\sim 30^\circ$ or less from vertical) with a possible orientation from northeast to southwest.

3.4. Moscoviense

Previous work suggests that Moscoviense (with main ring diameter of 445 km centered at 147°E , 26°N according to Table 1) is the result of an impact onto a preexisting larger basin (Ishihara et al., 2011; Neumann et al., 2015). The preexisting basin (referred to as “Moscoviense North”) has a main ring diameter of 640 km offset about 80 km to the northwest of Moscoviense itself. This ring is visible in the shaded relief background map of Figure 2a. An inner 192-km diameter partial peak ring is nearly concentric with the main ring of the basin (see Figure S16 of Neumann et al. [2015]). The inner peak ring encloses a strong Bouguer gravity anomaly and marks the probable boundary of the impact melt pool.

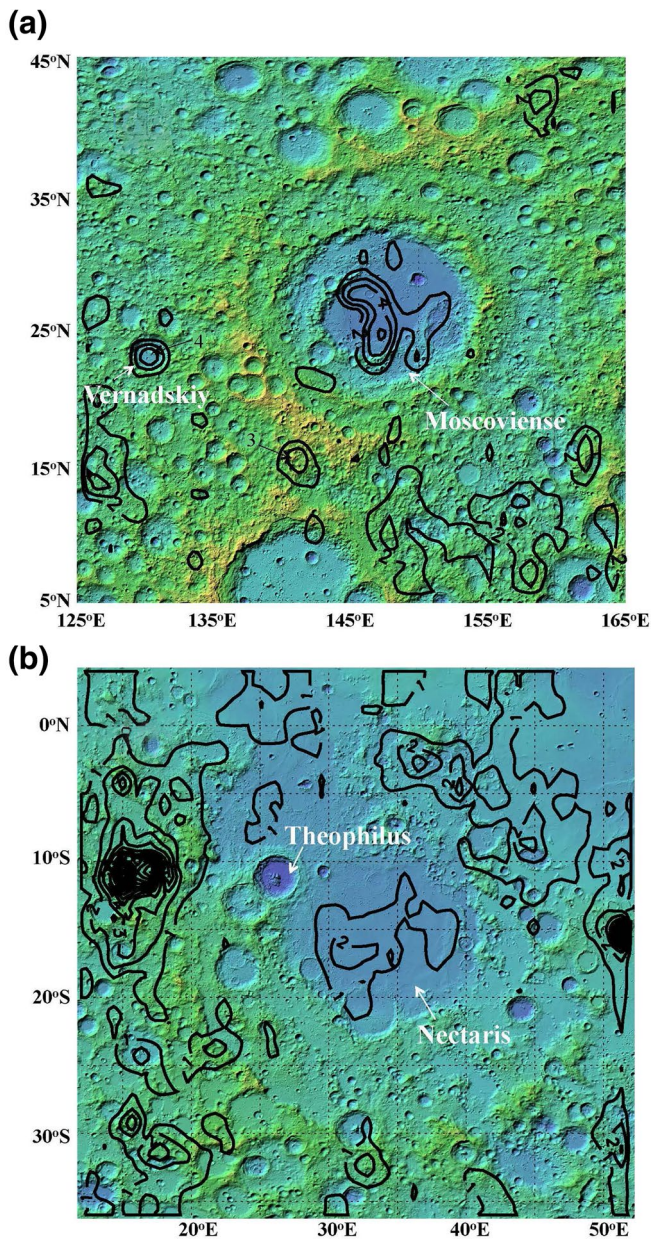


Figure 2. As in Figure 1 but for two other Nectarian-aged basins: (a) Moscoviense; and (b) Nectaris.

& Wieczorek, 2017; and references therein), the present approach complements that prior work in several ways. The inversion method that is employed is that of Parker (1991) which was originally applied to study the magnetization of seamounts. Details of the method are described, for example, by Oliveira and Wieczorek (2017). This method makes no assumptions about the shapes, volumes, or locations of magnetic sources. It only assumes that the direction of magnetization is constant within the volumetric region that is analyzed.

4.1. Crisium

Figure 3 plots the field magnitude and the three vector field components at 25 km altitude over the Crisium basin according to the ESD solution described in Section 3.1. Two main anomalies are present, referred to

Figure 2a is a map of the field magnitude in equirectangular (equidistant cylindrical) projection over shaded relief for a 40° by 40° region centered on the Moscoviense basin. It was produced using an ESD technique similar to that applied to produce Figures 1a and 1c above. The mapping altitude was again 25 km and the contour interval is 1 nT. The maximum mapped anomaly amplitude at this altitude is ~5 nT. The data employed consisted of both LP data from May of 1999 (May 27, 0.1 h to May 30, 17.5 h) and KG data from June of 2009 (June 5, 11.0 h to June 7, 0.9 h). These data were more carefully selected than those used to construct Figure S1, which only used LP data from May of 1999.

As seen in Figure 2a, the main Moscoviense magnetic anomaly is centered on the east-northeast side of the inner peak ring and follows approximately the curvature of the ring. It is consistent with a moderately oblique impact along a trajectory from west-southwest to east-northeast. No magnetic signature in the interior of the preexisting Moscoviense North basin would remain because the later Moscoviense impact would have thermally erased it.

3.5. Nectaris

Nectaris is one of three “certain” multiringed lunar impact basins (Neumann et al., 2015) and marks the base of the Nectarian epoch. It is superposed on the southeastern edge of a preNectarian basin, Asperitatis. The main ring diameter of about 860 km is easily visible in the shaded relief of Figure 2b. An inner ring with diameter 440 km bounds the inner mare fill and contains a strong Bouguer gravity anomaly (see Figure S4 of Neumann et al.).

Figure 2b is a map of the field magnitude at 25 km altitude produced in a manner similar to those of Figures 1a, 1c, and 2a. It is in equirectangular projection superposed on LROC WAC shaded relief. The 61 by 61 ESD dipole array was again placed at 10 km depth and KG data from May 2009 were used (May 16, 13.2 h to May 19, 15.0 h).

The strongest part of the internal magnetic anomaly has an amplitude of about 2.5 nT at this altitude and is displaced toward the southwestern side of the inner ring. An impactor trajectory of northeast to southwest at an angle from the vertical of less than roughly 45° is therefore suggested.

4. Inversion Modeling

As discussed in the Introduction, while a number of other groups have previously modeled lunar magnetic anomalies to infer directions of magnetization and paleomagnetic pole positions (Baek et al., 2019; Oliveira

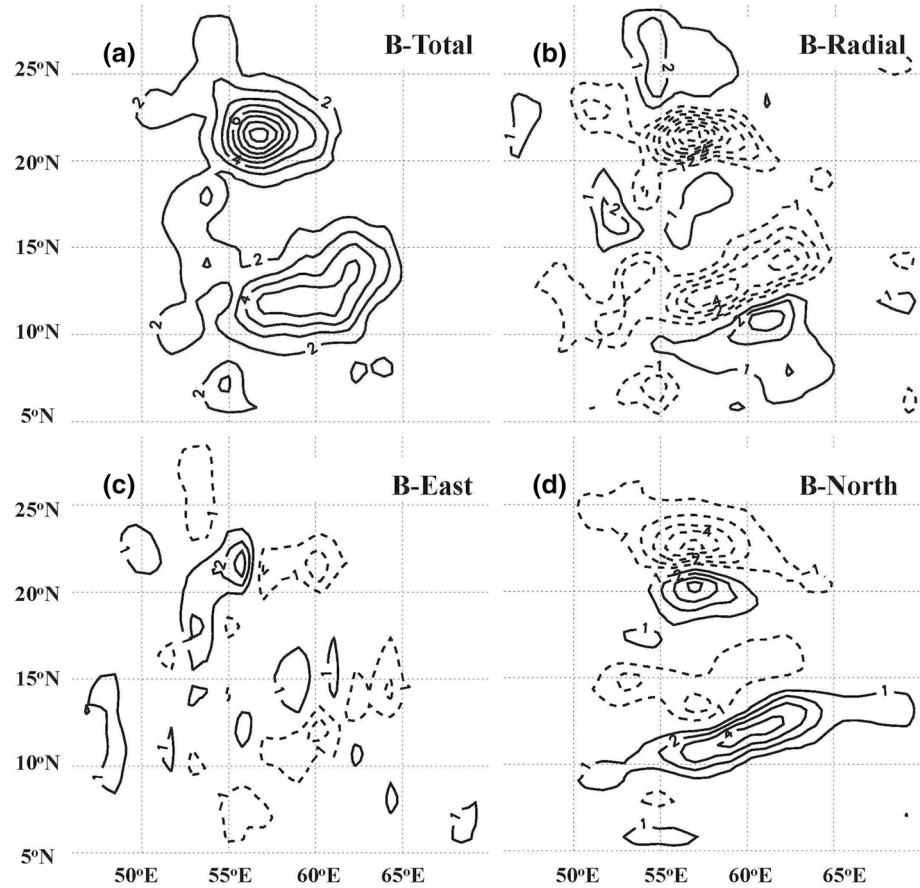


Figure 3. Equivalent source dipole (ESD) model (a) magnetic field magnitude and (b–d) vector field components at a constant altitude of 25 km over the Crisium basin. Contour interval: 1 nT; in (a), contours begin at 2 nT; in (b–d), contours begin at 1 and –1 nT.

here as the northern and southern anomalies. The northern anomaly is stronger (~ 9 nT), more compact, and more dipolar. However, the southern anomaly is also relatively strong (~ 5.5 nT) and is separated sufficiently from nearby anomalies so that it can be modeled. Given that there are two distinct strong anomalies within Crisium, the two anomaly sources may not necessarily be magnetized uniformly in one direction. To test this possibility, Parker’s method was applied independently to the two source regions.

A first estimate for the directions of magnetization of the two anomaly sources can be obtained from an inspection of the field component plots in Figure 3. The northern anomaly radial component peak of ~ -8 nT nearly coincides with the field magnitude maximum of 9 nT while the north component plot shows a stronger negative (southward) maximum of ~ -5 nT than the positive (northward) maximum of ~ 4 nT. This implies that the vector is mainly radially inward but is tilted slightly toward the north. The southern anomaly radial maximum of ~ -4 nT mostly coincides with the field magnitude maximum of ~ 5.5 nT while the north component plot shows a northward maximum of ~ 4 nT that is, larger than the southward maximum of ~ -2 nT. This implies that the southern source vector is radially inward but is tilted toward the south.

These expectations are confirmed by applications of Parker’s method as summarized in the first two rows of Table 2. The best fitting direction of magnetization is expressed in two forms. First, magnetic inclination (Inc or dip) and declination (Dec), direction angles inherited from geomagnetism, are given in column 3 with definitions given below the table. However, these angles are less than ideal for the Moon, which has no global field at present. For better visualization, an alternate pair of direction angles, α and β , which are based on a local spherical coordinate system, are therefore given in column 4. α is the angle made by the magnetization vector with the zenith ($\alpha = \text{Inc} + 90^\circ$). β is the azimuth angle of the surface projection of

Table 2
Summary of Inversion Modeling Results

Anomaly name and data source	Peak location	Best fit direction ^a , Inc, Dec.	Best fit direction ^b , α , β	Best fit north paleopole	RMS misfit, Norm. ^c
Crisium northern, LP	56°E, 22°N	70°, 7°	160°, 83°	243°E, 58°S	0.07
Crisium southern, LP	59°E, 13°N	18°, 169°	108°, 281°	268°E, 66°N	0.09
Humboldtianum, LP	79°E, 58°N	−28°, 327°	62°, 123°	114°E, 13°S	0.10
Mendel-Rydberg, KG	264°E, 52°S	−70°, 300°	20°, 150°	326°E, 54°S	0.05
Moscoviense, LP	147°E, 25°N	28°, 343°	118°, 107°	205°E, 71°S	0.14
Nectaris, KG	32°E, 17°S	52°, 159°	142°, 291°	259°E, 65°N	0.20

^aInc and Dec are magnetic inclination (angle relative to the surface, positive downward) and declination (azimuth angle of the vector surface projection measured clockwise from north). ^b α is the angle made by the magnetization vector with the zenith; β is the azimuth angle of the vector surface projection measured counter-clockwise from east. ^cListed are RMS misfits normalized by the peak mapped anomaly amplitudes as follows: Crisium northern: 9 nT; Crisium southern: 5.5 nT; Humboldtianum: 3 nT; Mendel-Rydberg: 7 nT; Moscoviense: 5 nT; Nectaris: 2.5 nT.

the vector measured counter-clockwise from east ($\beta = 90^\circ - \text{Dec}$). As seen in the first row of the table, the best-fitting direction of magnetization for the northern anomaly source is 70° downward from horizontal with surface projection about 7° east of north. As seen in the second row, the best-fitting southern anomaly source direction is about 18° downward from horizontal with surface projection about 11° east of south.

Further details of the application of Parker's method to the northern and southern anomalies are shown in Figures 4 and 5 and in Figures S2–S5 of the supporting material. The inversions were done using the same radial field component data used in the construction of Figure 3. The top center plots of Figures 4 and 5 show the observed magnetic field magnitude along the orbit tracks. Vertically oriented model dipoles were placed within the inner dashed black circles of the top right plots of both figures. The amplitude of each nonzero dipole moment is indicated by the color scale. The locations of the strongest dipoles correlate closely with the field magnitude shown in the top center plots. The inversion considers only observations within the outer solid black circles. The final model radial field component agrees well with the observed radial field component as shown in the bottom three plots of both figures. Figures S2 and S4 of the SM show the final model field magnitude and the three vector field components for the two analyses. Figures S3 and S5 are plots of the RMS misfit versus north paleomagnetic pole position.

The RMS misfits for the best-fitting direction and pole position for the northern and southern anomalies were 0.65 nT and 0.50 nT, respectively. However, the effective level of confidence in a given anomaly inversion depends also on the anomaly amplitude such that stronger anomalies are less likely to be affected by external fields than are weaker anomalies. To take this into account, column 6 of Table 2 lists the RMS misfits normalized by peak anomaly amplitude. The normalized misfit for the northern anomaly is 0.07 while that for the southern anomaly is 0.09.

The preferred directions of magnetization of the northern and southern anomaly sources differ by roughly 90° . As seen in column 5 of Table 2, their corresponding best-fitting paleomagnetic pole positions are more than 120° apart. The two north paleopoles are at comparable longitudes (243°E and 268°E) and are at high latitudes (58°S and 66°N , respectively) but are in opposite hemispheres. This large difference invalidates any application of Parker's method to both anomalies simultaneously since the method assumes a constant direction of magnetization throughout the region being inverted.

A physical understanding of the Crisium anomaly pole position locations (and those of other anomalies to be discussed below) can be obtained by considering Figure 6. The northern anomaly source direction is inward and tilted slightly northward, similar to that of the red arrow in the figure. The curvature of dipolar field lines requires that the south magnetic pole position must be displaced northward along a great circle from the anomaly location by an angle p :

$$p = \tan^{-1}(\text{abs}(2 \tan \alpha)) \quad (1)$$

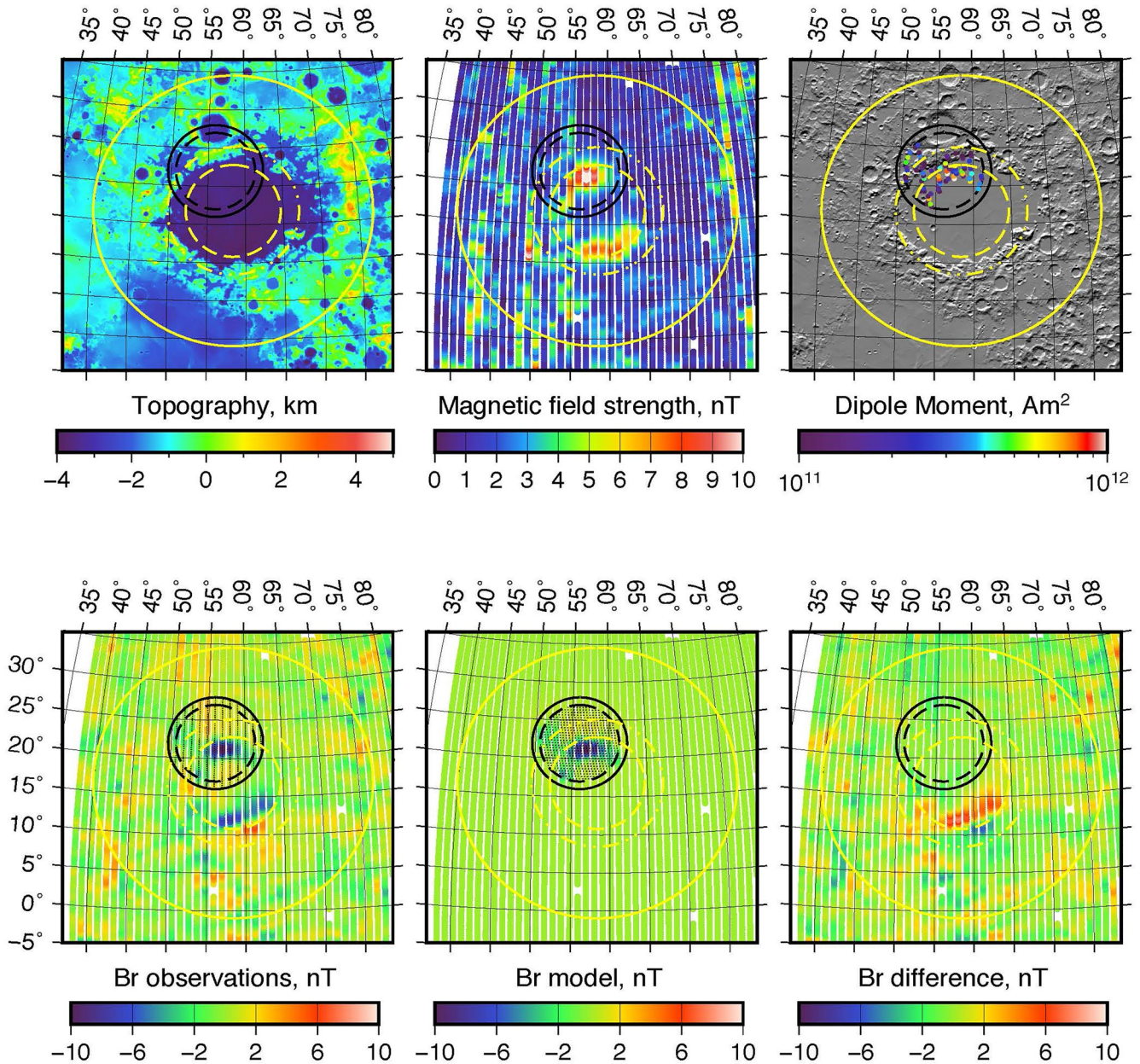


Figure 4. Inversion modeling summary for the northern Crisium anomaly. In each figure, the solid yellow circle is the outer ring, the dot-dashed yellow circle is the inner ring, and the dashed yellow circle is the inner depression (Neumann et al., 2015). The black outer circle encloses the observations that are considered in the inversion. The black dashed inner circle encloses the region where model dipoles are allowed. Top left: LOLA topography; Top center: magnetic field magnitude at the spacecraft altitude along selected Lunar Prospector (LP) orbit segments from March 1999; Top right: model dipoles with nonzero magnetic moments indicated; Bottom left: observed radial field component at spacecraft altitude; Bottom center: model radial field component; Bottom right: model minus observed radial field difference.

where $\alpha (= \text{Inc} + 90^\circ)$ is the direction angle relative to the zenith defined above. Equation 1 follows from the standard formula for dipolar field lines (e.g., Butler, 1992). For $\alpha = 70^\circ$, $p = 36^\circ$. Neglecting the small difference from north of the magnetization vector surface projection, the south magnetic pole must therefore be at a latitude of about 58°N . The north magnetic pole is therefore at about 58°S at a longitude about 180° away from the anomaly longitude, which agrees approximately with the location given in Table 2, column 5. More complete formulas for calculating the north paleomagnetic pole position when the source location and direction of magnetization are known are given in Hood and Zakharian (2001), after Butler (1992).

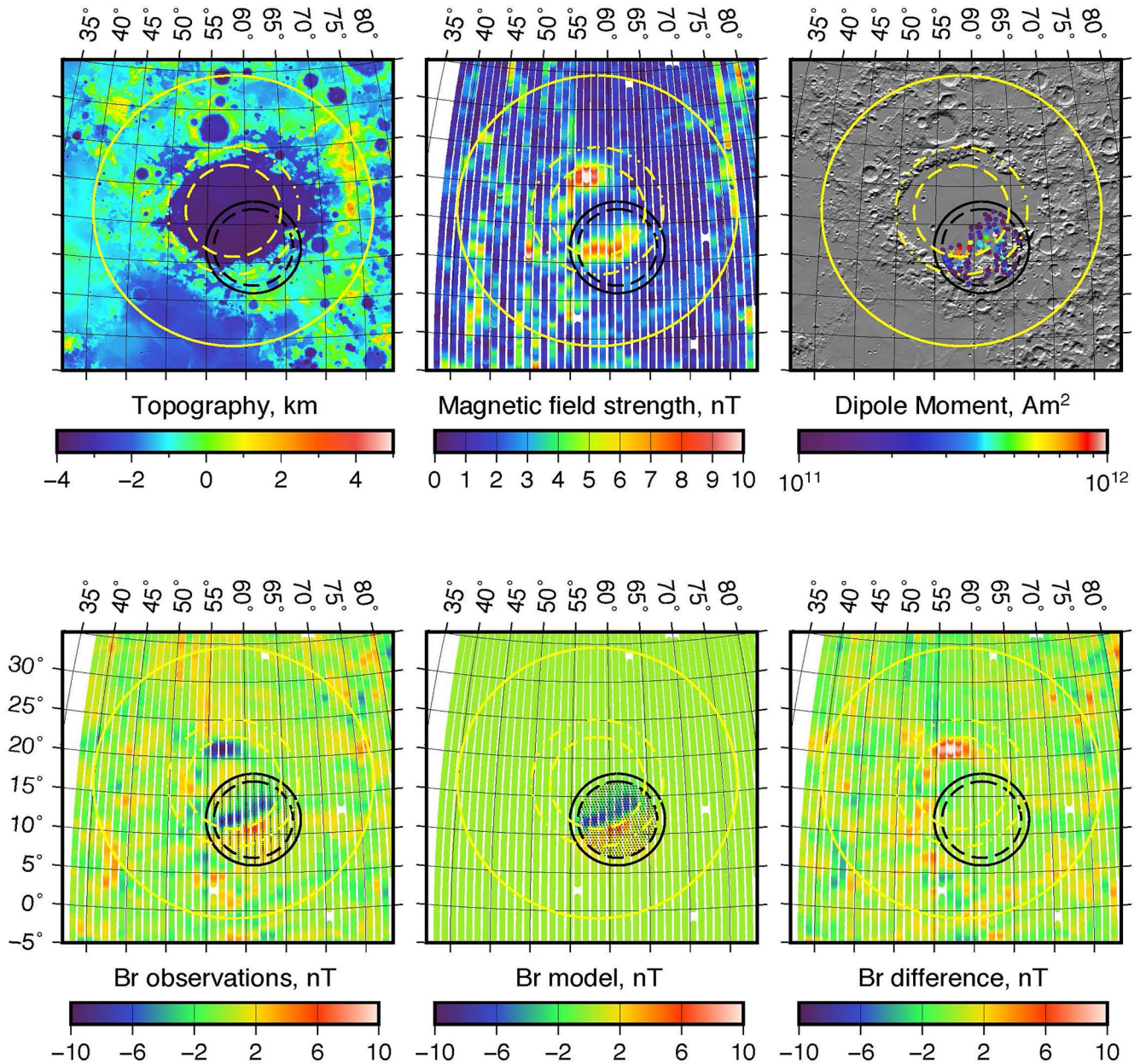


Figure 5. As in Figure 4 but for the southern Crisium anomaly.

4.2. Humboldtianum

Figure 7 plots the field magnitude and three vector field components at 25 km altitude over the Humboldtianum basin in the same format as Figure 3. A single broad maximum (~ 3 nT) is centered at about 79°E , 58°N . The radial component maximum of ~ 2.5 nT coincides approximately with the field magnitude maximum implying that the radial component of the magnetization vector is outward. However, the north component plot has a southward maximum located southeast of the northward maximum with a somewhat larger amplitude, implying that the vector is tilted toward the northwest.

This qualitative expectation is supported by the Parker's method results listed in the third row of Table 2. The best-fit direction is tilted 28° outward from the horizontal with a surface projection 33° west of north. The Parker model radial field component agrees well with the observed radial field component as shown in Figure 8. The normalized RMS misfit for this anomaly is 0.10 (column 6 of Table 2), only slightly larger

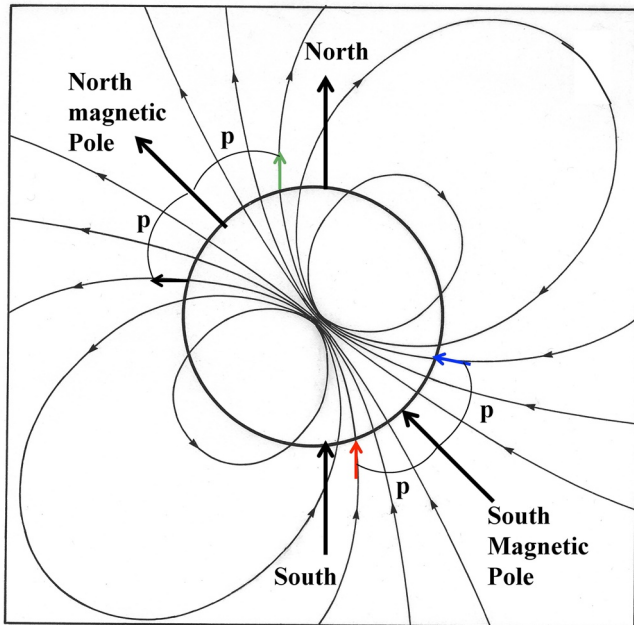


Figure 6. Diagram illustrating the relationship between the tilt of a magnetization vector and the location of the north or south paleomagnetic pole. For an inward vector tilted northward (red arrow), the south paleomagnetic pole is displaced northward by an angle p . For an inward vector tilted southward (blue arrow), the south paleomagnetic pole is displaced southward by angle p . Similar relationships hold between the tilt of an outward magnetization vector and the location of the north paleomagnetic pole. See the text.

than that for the southern Crisium anomaly. The remaining model vector field components and the model field magnitude are shown in Figure S6.

According to Figure 6, a northwestward tilted outward magnetization vector requires a north magnetic pole position displaced southwestward from the anomaly location. For $\alpha = 62^\circ$, the great circle arc distance to the pole is $p = 75^\circ$. In agreement with this expectation, the best-fitting north paleomagnetic pole position listed in column 5 is at 114°E , 13°S . A plot of the RMS misfit versus north paleopole location is shown in Figure S7. The RMS misfit at the best-fitting location is 0.30 nT. There is a fairly distinct minimum in the RMS misfit at the paleopole location just south of the equator. It is therefore difficult to avoid the conclusion that the Humboldtianum anomaly requires a low-latitude (i.e., near-equatorial) paleopole.

4.3. Mendel-Rydberg

Figure 9 plots the observed field magnitude and the three vector field components at 25 km altitude over the Mendel-Rydberg basin obtained from the ESD solution described in Section 3.3. The Mendel-Rydberg anomaly is characterized by a relatively strong positive radial component maximum with an amplitude exceeding 6 nT that nearly coincides with the field magnitude maximum of ~ 7 nT. The north field component has a larger southward maximum than northward maximum located southeast of the northward maximum indicating a magnetization vector that is, radially outward but tilted toward the northwest. Consistently, as seen in the fourth row of Table 2, the best-fitting magnetization vector obtained by applying Parker's method to this anomaly is inclined 70° above the horizontal with a surface projection oriented 30° north of west. The RMS misfit is 0.35 nT and the normalized misfit is 0.05 (column 6 of Table 2).

This is the lowest normalized misfit of the six inversions, due to both a strong anomaly amplitude and a relatively simple dipolar structure for the anomaly. Figure S8 shows the distribution of model dipoles and compares the observed and modeled radial field component maps at constant altitude for this basin. Figure S9 plots the model field components.

Given the best-fitting magnetization direction with $\alpha = 20^\circ$, one expects a north paleopole located $p = 36^\circ$ along a great circle path toward the east-southeast. As seen in Table 2 (fourth row, column 5), the calculated north paleopole is at 326°E , 54°S . Figure S10 plots the RMS misfit versus paleopole location. The north paleopole is therefore at moderately high southern latitudes.

4.4. Moscoviense

Figure 10 plots the field magnitude and three vector field components over Moscoviense at 25 km altitude according to the ESD solution described in Section 3.4. The radial component maximum has a negative peak near the field magnitude maximum and a positive peak northwest of the field magnitude maximum. The north field component plot has a dominant negative anomaly and a smaller positive anomaly south-southwest of the negative anomaly. One therefore expects a magnetization vector that is, radially inward but tilted toward the north-northwest. As seen in the fifth row of Table 2, the best-fitting direction obtained from the Parker's method analysis is 28° below horizontal with surface projection oriented 17° west of north. The RMS misfit is 0.71 nT (column 6 of the table). For $\alpha = 118^\circ$, $p = 75^\circ$ so, comparing with the red arrow in Figure 6, the south paleomagnetic pole should lie about 75° of arc along a great circle path toward the north-northwest. This estimate agrees with the north paleopole listed in Table 2, column 5. The north paleopole is at 205°E , 71°S . The corresponding south paleopole is at 25°E , 71°N .

Details of the application of Parker's method to the Moscoviense anomaly are shown in Figures S11–S13 of the SM. As seen in the top right plot of Figure S11, all nonzero model dipoles lie within or on the partial

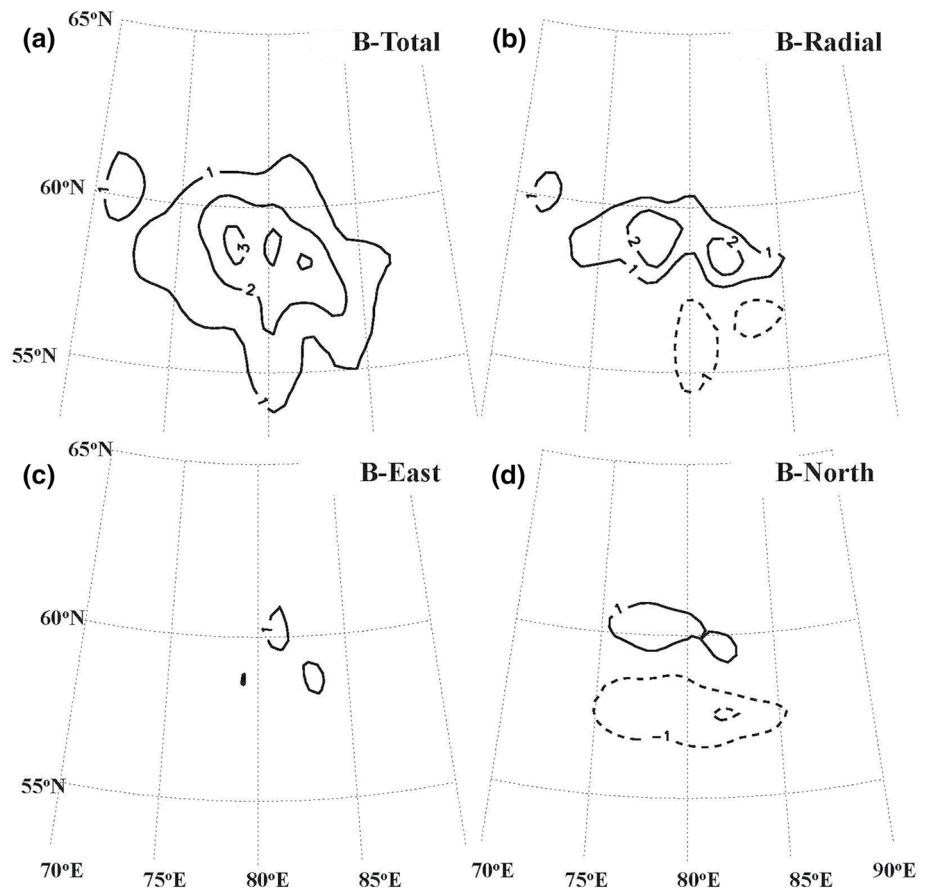


Figure 7. As in Figure 3 but for the Humboldtianum anomaly.

inner peak ring of the basin. They produce a model radial field component that agrees well with the observed radial field component as shown in the bottom three plots of the figure. Figure S13 shows that the RMS misfit reaches a minimum for a high southern latitude paleopole, although the minimum is not very distinct. The normalized misfit in Table 2 is 0.14.

4.5. Nectaris

Figure 11 plots the field magnitude and vector field components of the Nectaris anomaly at 25 km altitude obtained from the ESD solution described in Section 3.5. This is a less intense intrinsic anomaly (peak mapped amplitude ~ 2.5 nT) than those in the other four selected basins. The radial field peak of ~ -2 nT lies close to the field magnitude maximum and is elongated in the northeast-southwest direction. A positive radial component anomaly with amplitude ~ 1.5 nT is elongated parallel to the negative radial anomaly. The north component anomaly is mainly positive as seen in the (d) part of the figure while the east component shows almost no anomaly. These characteristics lead one to expect a magnetization vector that is, mainly downward with surface projection toward the south or south-southeast. The Parker inversion solution listed in the sixth row of Table 2 agrees with this expectation. The best-fitting vector is downward at an angle of 52° from the horizontal with surface projection 21° east of south. The minimum RMS misfit was 0.49 nT but the relatively low anomaly peak amplitude yields a normalized misfit of 0.20, which is the largest of the six inversions. The southward tilt of the vector is comparable to that of the blue arrow in Figure 6. For $\alpha = 142^\circ$, one therefore expects a south paleopole located about 57° of arc along a great circle toward 21° east of south. The north paleomagnetic pole is diametrically opposite this location at 259°E , 65°N , as listed in column 5 of Table 2. Further details of the Parker inversion solution for the Nectaris anomaly are given in Figures S14–S16 of the SM.

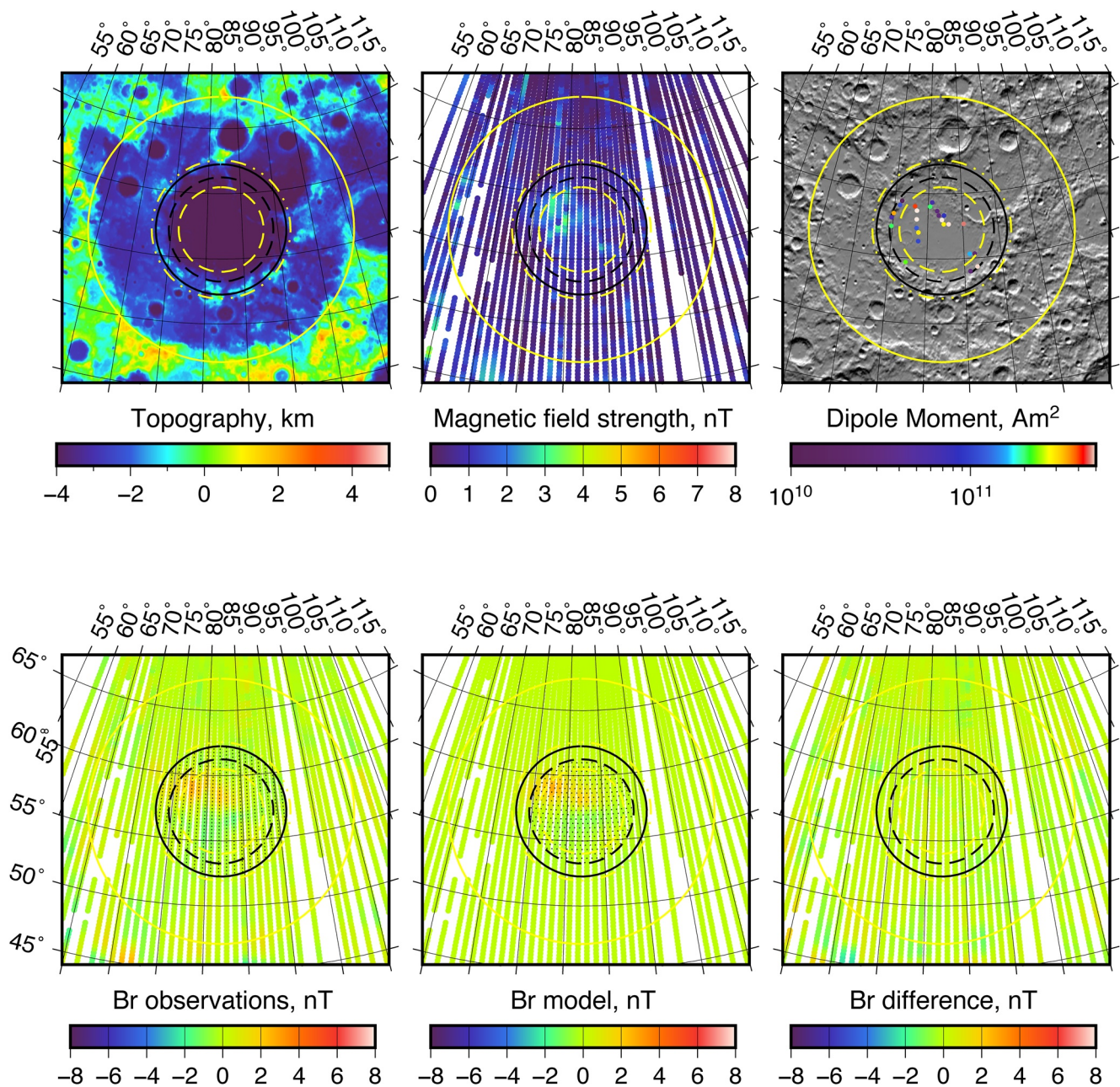


Figure 8. As in Figures 5 and 6 but for the Humboldtianum anomaly. Selected LP orbit segments from April 1999 are used (see the text).

5. Summary and Discussion

As described in Section 2, a recent large-scale map of the lunar crustal magnetic field (Figure S1) allows improved selection of ringed impact basins that most confidently contain intrinsic internal anomalies. Magnetic anomalies in the near vicinities of 25 candidate basins were examined using the large-scale map, supplemented by regional maps for several basins in the polar regions. Of the 25 basins, 18 were found to contain anomalies within their inner rims. However, in most cases, these anomalies were not clearly separated from anomalies outside the rims that were of equal or larger amplitude and that could be a consequence of magnetized ejecta deposition from later basin-forming impacts. Only five basins were confidently considered to contain intrinsic internal anomalies, i.e., anomalies with sources that formed within the basin inner rim at a time following the impact that produced the basin. These include four basins previously recognized

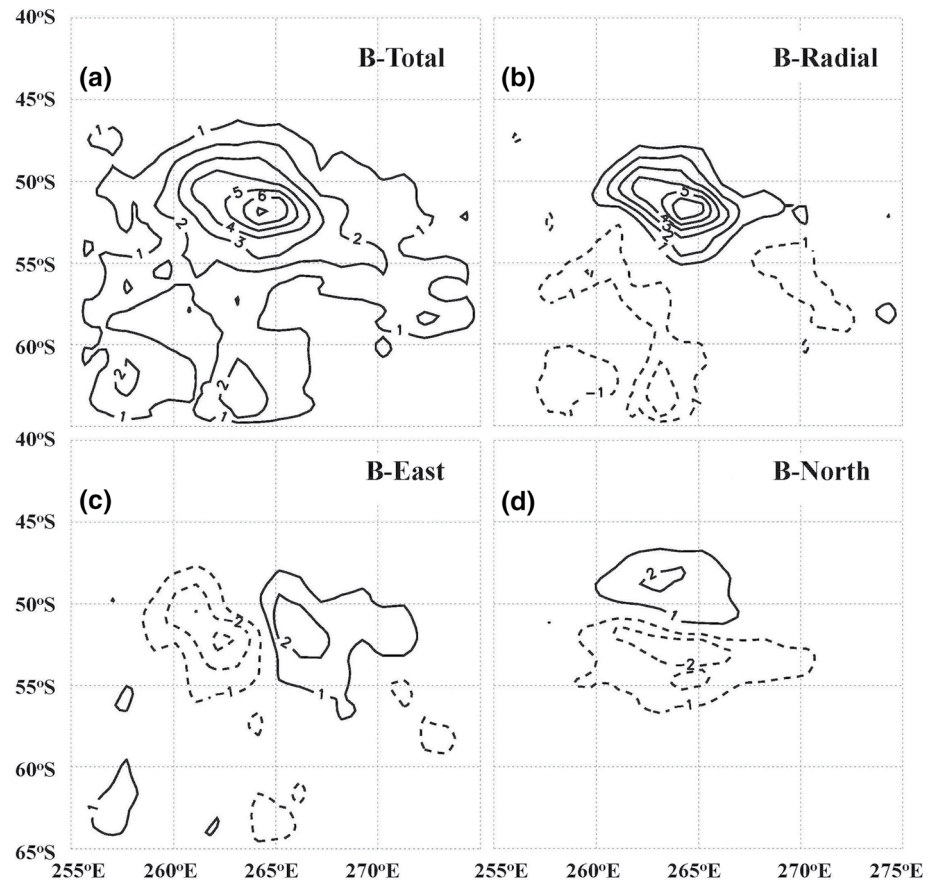


Figure 9. As in Figure 3 but for the ESD model magnetic field magnitude over the Mendel-Rydberg impact basin (contour interval: 1 nT; zero contours are not plotted).

to have such anomalies (Crisium, Humboldtianum, Mendel-Rydberg, and Moscoviense; e.g., Hood, 2011) plus one additional basin (Nectaris). Several other basins (Schrödinger, Bailly, Serenitatis, Humorum, and Smythii) contain internal anomalies with marginally intrinsic characteristics but these are conservatively excluded here. Future geologic studies are needed to determine more confidently the origin of these anomaly sources.

All five of the selected basins are Nectarian in age (in agreement with Halekas et al. [2003]) but have no other obviously distinguishing characteristics. If future work confirms that anomalies in Schrödinger and Smythii are intrinsic, then there would be less compelling evidence for a dependence on basin age. It would then be possible that properties of the impactor (iron content) and its trajectory (combined with the existence of an ambient magnetizing field) dominantly determined whether a basin contains intrinsic internal anomalies or not. This possibility would be consistent with observations of intrinsic internal anomalies in some impact basins on Mercury but not in others of comparable age (Hood et al., 2018).

As discussed in the Introduction, likely sources of the identified intrinsic internal anomalies are impact melt rocks that are enriched in impactor iron. If so, then the observed anomaly distribution within a given basin combined with previous numerical simulations of impacts of iron-rich planetesimals on the Moon provide a means of constraining the trajectory of the impactor that created that basin. However, as emphasized in Section 3, the previous simulations were done for an SPA-sized basin so the specific interpretation of impact angles from the observed anomaly distributions should be treated with caution.

Regional crustal field maps of the five selected basins (Figures 1 and 2) were constructed using refined data selection criteria. For three of the five selected basins (those except Humboldtianum and Mendel-Rydberg), intrinsic anomalies are not concentrated close to the center of the inner rim but are offset on one side. In

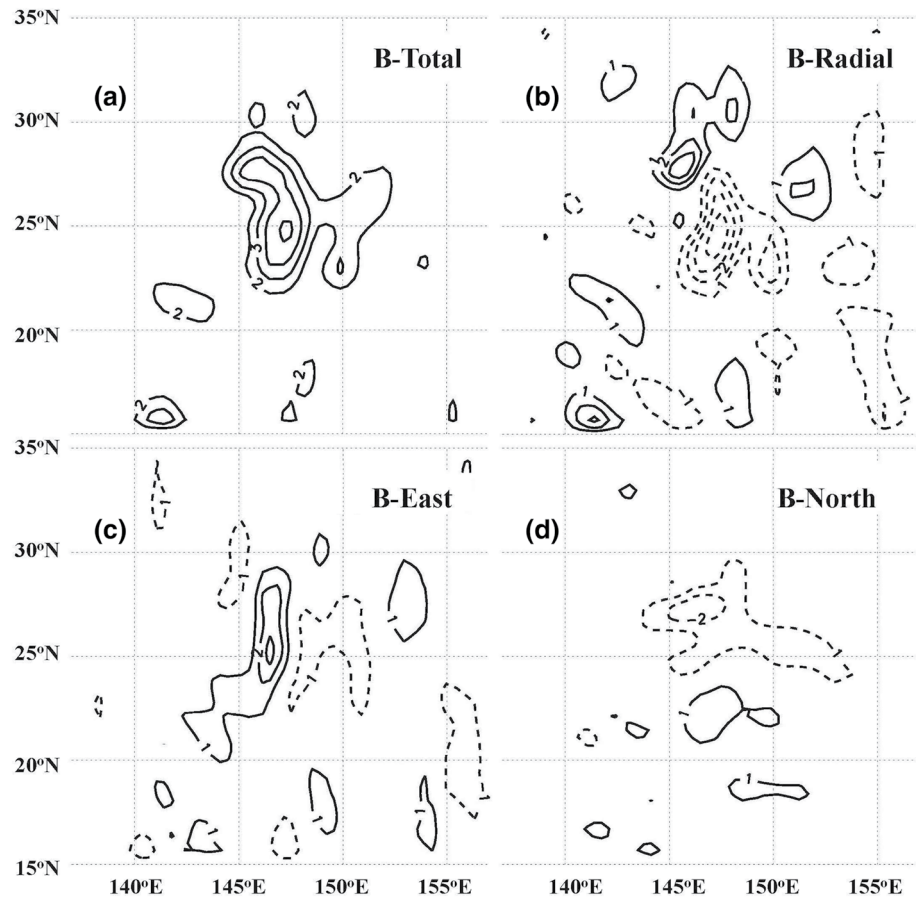


Figure 10. As in Figure 3 but for the Moscoviense basin. Both LP data from May of 1999 and Kaguya (KG) data from June of 2009 are used.

two of the latter basins (Crisium and Moscoviense), the internal anomalies follow approximately the curvature of the inner rim. The numerical simulations of Wieczorek et al. (2012), which were for the special case of the SPA basin, showed that a moderately oblique impact (impact angles between roughly 30° and 45° from vertical) of an iron-rich planetesimal could produce such an asymmetric distribution of impactor-added iron within the inner rim. Applying these results to the five selected basins, it is suggested that impactor trajectories were in all cases within $\sim 45^\circ$ of being vertical. Favored oblique impactor trajectories are east-northeast to west-southwest for Crisium, west-southwest to east-northeast for Moscoviense; and northeast to southwest for Nectaris. For Humboldtianum and Mendel-Rydberg, the trajectories were likely within 30° of vertical. But possible orientations are southeast to northwest for Humboldtianum at high northern latitudes and northeast to southwest for Mendel-Rydberg at high southern latitudes. At least a small tendency for the trajectories to lie nearly parallel to the lunar equatorial plane and the ecliptic may therefore be inferred. However, these results do not favor a primeval lunar satellite origin for the impactors (Runcorn, 1983) since nearly grazing impacts would be expected if they were pulled into the Moon by tidal friction.

As reported in Section 4, applications of Parker's (1991) inversion method to selected direct magnetometer measurements over the intrinsic internal anomalies identified here (two in Crisium, one in each of the remaining four basins) yields directions of magnetization and north paleomagnetic pole positions listed in Table 2. In the case of the northern Crisium anomaly, the best-fitting direction of magnetization is 70° downward from horizontal with surface projection oriented 7° east of north. For comparison, an independent analysis of the same March 1999 LP magnetometer data for this anomaly assuming a point dipole source geometry obtains a best-fitting direction that is, 77° downward from horizontal with surface projection oriented 21° east of north (Baek et al., 2019; see their Table 1). The best-fitting direction of magnetization

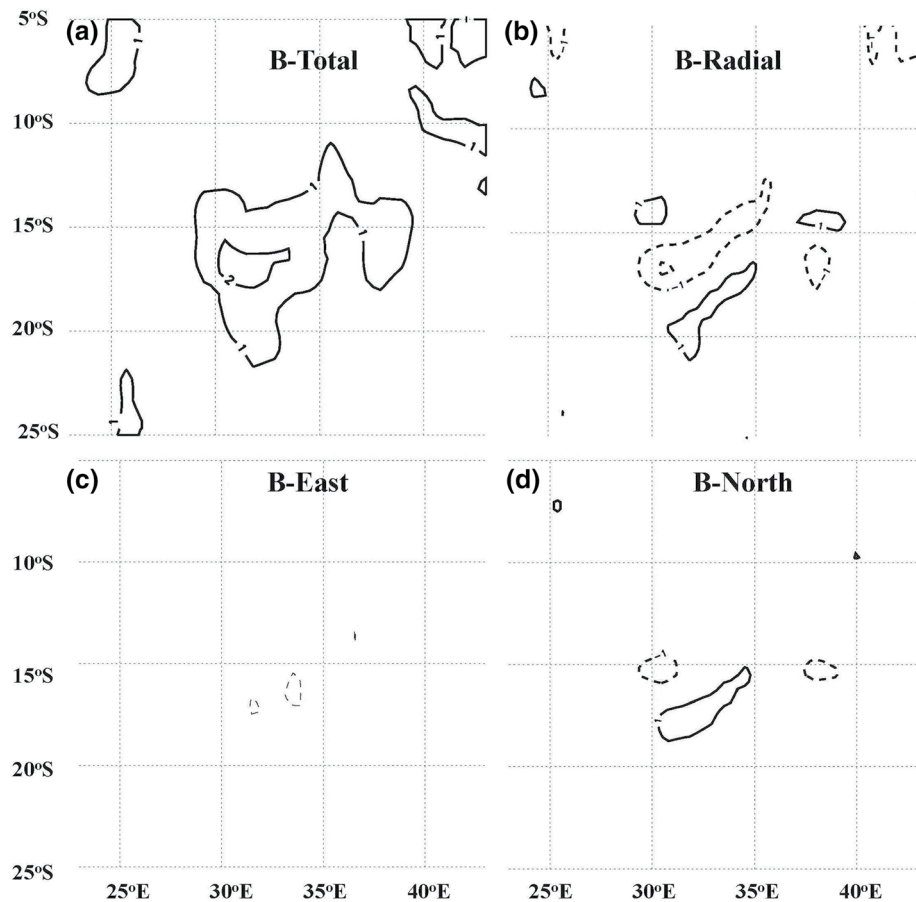


Figure 11. As in Figure 3 but for the ESD model magnetic field magnitude over the Nectaris impact basin. KG data from May of 2009 were used.

for the southern Crisium anomaly listed in Table 2 is 18° downward from horizontal with surface projection oriented 11° east of south. For comparison, an analysis of the same data by Baek et al. (2019) yields a preferred direction for the strongest of their two source dipoles of 12° downward from horizontal with surface projection oriented 14° east of south. Our analysis of the Crisium anomalies using Parker's method and the analysis by Baek et al. of the same anomalies are therefore in reasonable agreement. The inferred directions are roughly 90° apart and their corresponding paleomagnetic pole positions are more than 120° of arc apart.

The remaining four intrinsic internal basin anomalies analyzed in Section 4 using Parker's method yield paleomagnetic pole positions that are also listed in Table 2, column 5. Five of the six paleopoles are at latitudes higher than 50° but the Humboldtianum anomaly paleopole is nearly equatorial (best-fitting latitude, 13°S). Overall, the best-fitting paleomagnetic pole positions are widely scattered and are difficult to reconcile with a centered axially aligned dipolar magnetizing field as would be expected for a core dynamo. As concluded also by Oliveira and Wiczonek (2017), if the magnetizing field was a core dynamo field, the dipole axis was not aligned with the rotation axis and may have wandered quasirandomly. Moreover, given the disparate directions inferred for the two Crisium anomaly sources, the time scale for dynamo axis reorientation would be required to be less than the time interval between effective magnetization acquisition by the two sources.

Magnetization acquisition by an iron-enriched melt sheet on one side of the inner rim may have been delayed relative to that on the other side of the rim if the melt sheet was variable in thickness and therefore did not cool uniformly with time. Alternatively, the magnetization of one or the other of the anomaly sources may have been "reset" following a subsequent heating event such as internal mare volcanism.

The terrestrial Chicxulub basin, like Crisium, was apparently formed by a steeply inclined ($<45^\circ$ from vertical) impact (Collins et al., 2020). It has an inner rim diameter of ~ 150 km and an inner peak ring about

80 km across. While magnetic anomalies associated with terrestrial impact structures likely have a different origin than those within lunar basins (due to differences in magnetic carriers and magnetization mechanisms), direct drilling and seismic reflection data are available to characterize the melt sheet (for a review, see Gulick et al. [2013]). Results show that it has an impact melt sheet <3 km thick concentrated within the inner peak ring but with pockets of melt distributed in the annular trough between the peak ring and the inner rim. If similar azimuthal asymmetries exist in the impact melt distribution within the inner rim of Crisium, cooling rates may have differed significantly, possibly explaining the disparate magnetization directions of the northern and southern anomaly sources.

A more extreme possible explanation is that the internal magnetizing field was not a dipolar core dynamo at all. Instead, higher-order dynamo fields may have been generated in a basal magma ocean extending to fairly shallow (~200 km) depths (Scheinberg et al., 2018; see their Figure 1). Le Bars et al. (2011) have shown that the energy of a basin-forming impact is sufficient to modify the lunar rotation rate, producing large-scale fluid flows in the core and temporary enhanced dynamo field generation. The same energy could have powered localized dynamo action in a basal magma ocean or in smaller magma chambers. This scenario could potentially explain the different magnetization directions of the two Crisium anomaly sources even if they cooled nearly simultaneously. A source depth of the internal dynamo field comparable to the separation of the two anomalies (~240 km) would be needed.

Data Availability Statement

Supported at the University of Arizona by grant 80NSSC18K1602 from the NASA Lunar Data Analysis Program. Lunar Prospector calibrated magnetometer data are available from the Planetary Plasma Interactions node of the NASA Planetary Data System (<https://pds-ppi.igpp.ucla.edu>). Kaguya (SELENE) vector magnetometer data are available from the Japan Aerospace Exploration Agency (JAXA) at <http://darts.isas.jaxa.jp/planet/pdap/selene>. The shaded relief maps with Lunar Orbiter Laser Altimeter data superposed used in the construction of several figures are available from the U.S. Geological Survey in Flagstaff, Arizona (https://astrogeology.usgs.gov/search/map/Moon/LMMP/LOLA-derived/Lunar_LRO_LOLA_Clr-Shade_Global_128ppd_v04). The large-scale field map at 30 km altitude shown in Figure S1 (from Hood et al., 2021), including the three vector field components as well as the field magnitude is available for download from the Planetary Plasma Interactions node of the NASA Planetary Data System at UCLA (Hood et al., 2020; <https://doi.org/10.17189/1520494>).

Acknowledgments

We thank Drs. H. R. Kim and R. R. B. von Frese for helpful comparisons of magnetic anomaly inversion results during the early stages of this study. Finally, we thank the two anonymous reviewers and the associate editor for detailed criticisms that improved the final manuscript.

References

- Arkani-Hamed, J., & Boutin, D. (2014). Analysis of isolated magnetic anomalies and magnetic signatures of impact craters: Evidence for a core dynamo in the early history of the Moon. *Icarus*, 237, 262–277. <https://doi.org/10.1016/j.icarus.2014.04.046>
- Baek, S.-M., Kim, K.-H., Garrick-Bethell, I., & Jin, H. (2019). Magnetic anomalies within the Crisium basin: Magnetization directions, source depths, and ages. *Journal of Geophysical Research: Planets*, 124(2), 223–242. <https://doi.org/10.1029/2018JE005678>
- Butler, R. F. (1992). *Paleomagnetism: Magnetic domains to geologic terranes* (p. 319). Malden, MA: Blackwell Science.
- Carter, P. J., Leinhardt, Z. M., Elliott, T., Walter, M. J., & Stewart, S. T. (2015). Compositional evolution during rocky protoplanet accretion. *The Astrophysical Journal*, 813(1), 72. <https://doi.org/10.1088/0004-637X/813/1/72>
- Collins, G. S., Patel, N., Davison, T. M., Rae, A. S. P., Morgan, J. V., & Gulick, S. P. S. (2020). A steeply-inclined trajectory for the Chicxulub impact. *Nature Communications*, 11(1), 1480. <https://doi.org/10.1038/s41467-020-15269-x>
- Crawford, D. A. (2015). Computational modeling of electrostatic charge and fields produced by hypervelocity impact. *Proceedings of the 2015 Hypervelocity Impact Symposium, Procedia Engineering*, 103, 89–96. <https://doi.org/10.1016/j.proeng.2015.04.013>
- Crawford, D. A. (2020). Simulations of magnetic fields produced by asteroid impact: Possible implications for planetary paleomagnetism. *International Journal of Impact Engineering*, 137, 103464. <https://doi.org/10.1016/j.ijimpeng.2019.103464>
- Fassett, C. I., Head, J. W., Kadish, S. J., Mazarico, E., Neumann, G. A., Smith, D. E., & Zuber, M. T. (2012). Lunar impact basins: Stratigraphy, sequence and ages from superposed impact crater populations measured from Lunar Orbiter Laser Altimeter (LOLA) data. *Journal of Geophysical Research: Planets*, 117(E12), E00H06. <https://doi.org/10.1029/2011JE003951>
- Frey, H. (2011). Previously unknown large impact basins on the Moon: Implications for Lunar stratigraphy. *Recent Advances and Current Research Issues in Lunar Stratigraphy*, 477(March), (53–75). Boulder, CO: Geological Society of America Special Paper. [https://doi.org/10.1130/2011.2477\(02\)](https://doi.org/10.1130/2011.2477(02))
- Gattacceca, J., Boustie, M., Hood, L., Cuq-Lelandais, J.-P., Fuller, M., Bezaeva, N. S., et al. (2010). Can the lunar crust be magnetized by shock: Experimental groundtruth. *Earth and Planetary Science Letters*, 299(1–2), 42–53. <https://doi.org/10.1016/j.epsl.2010.08.011>
- Gilbert, G. K. (1893). The moon's face: A study of the origin of its features. *Bulletin of the Philosophical Society of Washington*, 12, 241–292.
- Gulick, S. P. S., Christeson, G. L., Barton, P. J., Grieve, R. A. F., Morgan, J. V., & Urrutia-Fucugauchi, J. (2013). Geophysical characterization of the Chicxulub impact crater. *Reviews of Geophysics*, 51(1), 31–52. <https://doi.org/10.1002/rog.20007>

- Halekas, J. S., Lin, R. P., & Mitchell, D. L. (2003). Magnetic fields of lunar multi-ring impact basins. *Meteoritics & Planetary Sciences*, 38(4), 565–578. <https://doi.org/10.1111/j.1945-5100.2003.tb00027.x>
- Halekas, J. S., Mitchell, D. L., Lin, R. P., Frey, S., Hood, L. L., Acuña, M. H., & Binder, A. B. (2001). Mapping of crustal magnetic anomalies on the lunar near side by the Lunar Prospector electron reflectometer. *Journal of Geophysical Research*, 106(E11), 27841–27852. <https://doi.org/10.1029/2000JE001380>
- Hart, R. J., Hargraves, R. B., Andreoli, M. A. G., Tredoux, M., & Doucouré, C. M. (1995). Magnetic anomaly near the center of the Vredefort structure: Implications for impact-related magnetic signatures. *Geology*, 23(3), 277–280. [https://doi.org/10.1130/0091-7613\(1995\)023<0277:MANTCO>2.3.CO;2](https://doi.org/10.1130/0091-7613(1995)023<0277:MANTCO>2.3.CO;2)
- Hemingway, D. J., & Tikoo, S. M. (2018). Lunar swirl morphology constrains the geometry, magnetization, and origins of lunar magnetic anomalies. *Journal of Geophysical Research: Planets*, 123(8), 2223–2241. <https://doi.org/10.1029/2018JE005604>
- Hood, L. L. (2011). Central magnetic anomalies of Nectarian-aged lunar impact basins: Probable evidence for an early core dynamo. *Icarus*, 211(2), 1109–1128. <https://doi.org/10.1016/j.icarus.2010.08.012>
- Hood, L. L. (2015). Initial mapping of Mercury's crustal magnetic field: Relationship to the Caloris impact basin. *Geophysical Research Letters*, 42, (December 11), 10565–10572. <https://doi.org/10.1002/2015GL066451>
- Hood, L. L. (2016). Magnetic anomalies concentrated near and within Mercury's impact basins: Early mapping and interpretation. *Journal of Geophysical Research: Planets*, 121(June 15), 1016–1025. <https://doi.org/10.1002/2016JE005048>
- Hood, L. L., & Artemieva, N. A. (2008). Antipodal effects of lunar basin-forming impacts: Initial 3D simulations and comparisons with observations. *Icarus*, 197(2), 485–502. <https://doi.org/10.1016/j.icarus.2007.08.023>
- Hood, L. L., Oliveira, J. S., Galluzzi, V., & Rothery, D. A. (2018). Investigating sources of Mercury's crustal magnetic field: Further mapping of MESSENGER magnetometer data. *Journal of Geophysical Research: Planets*, 123(10), 2647–2666. <https://doi.org/10.1029/2018JE005683>
- Hood, L. L., Richmond, N. C., & Spudis, P. D. (2013). Origin of strong lunar magnetic anomalies: Further mapping and examinations of LROC imagery in regions antipodal to young large impact basins. *Journal of Geophysical Research: Planets*, 118(6), 1265–1284. <https://doi.org/10.1002/jgre.20078>
- Hood, L. L., & Spudis, P. D. (2016). Magnetic anomalies in the Imbrium and Schrödinger impact basins: Orbital evidence for persistence of the lunar core dynamo into the Imbrian epoch. *Journal of Geophysical Research: Planets*, 121(11), 2268–2281. <https://doi.org/10.1002/2016JE005166>
- Hood, L. L., Torres, C. B., Oliveira, J. S., Wiczeorek, M. A., & Stewart, S. (2021). A new large-scale map of the lunar crustal magnetic field and its interpretation. *Journal of Geophysical Research: Planets*, 126. <https://doi.org/10.1029/2020JE006667>
- Hood, L. L., Torres, C. B., Oliveira, J. S., Wiczeorek, M. A., & Stewart, S. T. (2020). *Lunar crustal magnetic field map*. UCLA, Los Angeles, CA: NASA Planetary Data System. <https://doi.org/10.17189/1520494>
- Hood, L. L., & Zakharian, A. (2001). Mapping and modeling of magnetic anomalies in the northern polar region of Mars. *Journal of Geophysical Research*, 106(E7), 14601–14619. <https://doi.org/10.1029/2000JE001304>
- Hood, L. L., Zakharian, A., Halekas, J., Mitchell, D., Lin, R., Acuña, M., & Binder, A. (2001). Initial mapping and interpretation of lunar crustal magnetic anomalies using Lunar Prospector magnetometer data. *Journal of Geophysical Research*, 106(E11), 27825–27839. <https://doi.org/10.1029/2000JE001366>
- Ishihara, Y., Morota, T., Nakamura, R., Goossens, S., & Sasaki, S. (2011). Anomalous Moscoviense basin: Single oblique impact or double impact origin? *Geophysical Research Letters*, 38, L03201. <https://doi.org/10.1029/2010GL045887>
- Le Bars, M., Wiczeorek, M. A., Karatekin, Ö., Cébron, D., & Laneuville, M. (2011). An impact-driven dynamo for the early Moon. *Nature*, 479(7372), 215–218. <https://doi.org/10.1038/nature10565>
- Neumann, G. A., Zuber, M. T., Wiczeorek, M. A., Head, J. W., Baker, D. M. H., Solomon, S. C., et al. (2015). Lunar impact basins revealed by Gravity Recovery and Interior Laboratory measurements. *Science Advances*, 1(9), e1500852. <https://doi.org/10.1126/sciadv.1500852>
- Oliveira, J. S., & Wiczeorek, M. A. (2017). Testing the axial dipole hypothesis for the Moon by modeling the direction of crustal magnetization. *Journal of Geophysical Research: Planets*, 122(2), 383–399. <https://doi.org/10.1002/2016JE005199>
- Oliveira, J. S., Wiczeorek, M. A., & Kletetschka, G. (2017). Iron abundances in lunar impact basin melt sheets from orbital magnetic field data. *Journal of Geophysical Research: Planets*, 122(12), 2429–2444. <https://doi.org/10.1002/2017JE005397>
- Oran, R., Weiss, B. P., Shprits, Y., Miljkovic, K., & Tóth, G. (2020). Was the moon magnetized by impact plasmas? *Science Advances*, 6(40), eabb1475. <https://doi.org/10.1126/sciadv.abb1475>
- Parker, R. L. (1991). A theory of ideal bodies for seamount magnetization. *Journal of Geophysical Research*, 96(B10), 16101–16112. <https://doi.org/10.1029/91JB01497>
- Pilkington, M., & Grieve, R. A. F. (1992). The geophysical signature of terrestrial impact craters. *Reviews of Geophysics*, 30(2), 161–181. <https://doi.org/10.1029/92RG00192>
- Purucker, M. E., Head, J. W., III, & Wilson, L. (2012). Magnetic signature of the lunar South Pole-Aitken basin: Character, origin, and age. *Journal of Geophysical Research: Planets*, 117, E05001. <https://doi.org/10.1029/2011JE003922>
- Richmond, N. C., Hood, L. L., Halekas, J. S., Mitchell, D. L., Lin, R. P., Acuña, M., & Binder, A. B. (2003). Correlation of a strong lunar magnetic anomaly with a high-albedo region of the Descartes mountains. *Geophysical Research Letters*, 30(7), 1395. <https://doi.org/10.1029/2003GL016938>
- Runcorn, S. K. (1983). Lunar magnetism, polar displacements and primeval satellites in the Earth-Moon system. *Nature*, 304(5927), 589–596.
- Scheinberg, A. L., Soderlund, K. M., & Elkins-Tanton, L. T. (2018). A basal magma ocean dynamo to explain the early lunar magnetic field. *Earth and Planetary Science Letters*, 492(June 15), 144–151. <https://doi.org/10.1016/j.epsl.2018.04.015>
- Schultz, P. H., & Stickle, A. M. (2011). Arrowhead craters and tomahawk basins: Signatures of oblique impacts at large scales. *Paper presented at 42nd Lunar and Planetary Science Conference (Abstract 2611)*. Houston: Lunar & Planetary Institute.
- Shoemaker, E. M. (1962). Interpretation of lunar craters. In Z. Kopal (Ed.), *Physics and astronomy of the Moon* (pp. 283–359). New York and London: Academic Press.
- Smith, D. E., Zuber, M. T., Neumann, G. A., Lemoine, F. G., Mazarico, E., Torrence, M. H., et al. (2010). Initial observations from the Lunar Orbiter Laser Altimeter (LOLA). *Geophysical Research Letters*, 37(18), L18204. <https://doi.org/10.1029/2010GL043751>
- Takahashi, F., Tsunakawa, H., Shimizu, H., Shibuya, H., & Matsushima, M. (2014). Reorientation of the early lunar pole. *Nature Geoscience*, 7(6), 409–412. <https://doi.org/10.1038/NCEO2150>
- Tsunakawa, H., Shibuya, H., Takahashi, F., Shimizu, H., Matsushima, M., & Matsuoka, A. (2010). Lunar magnetic field observation and in situ global mapping of lunar magnetic anomalies by MAP-LMAG onboard SELENE (Kaguya). *Space Science Reviews*, 154(May 4), 219–251. <https://doi.org/10.1007/s11214-010-9652-0>

- Weiss, B. P., & Tikoo, S. (2014). The lunar dynamo. *Science*, *346*(6214), 1198–1209. <https://doi.org/10.1126/science.1246753>
- Wieczorek, M. A. (2018). Strength, depth, and geometry of magnetic sources in the crust of the Moon from localized power spectrum analysis. *Journal of Geophysical Research: Planets*, *123*(1), 291–316. <https://doi.org/10.1002/2017JE005418>
- Wieczorek, M. A., Weiss, B. P., & Stewart, S. T. (2012). An impactor origin for lunar magnetic anomalies. *Science*, *335*(6073), 1212–1215. <https://doi.org/10.1126/science.1214773>
- Wilhelms, D. E. (1984). Moon. In M. Carr (Ed.), *The geology of the terrestrial planets* (pp. 107–205). Washington, DC: NASA Science and Technology Information Branch.